Ramsey envelope modulation in NV diamond magnetometry

Jner Tzern Oon [1,2,*,†] Jiashen Tang [1,2,†] Connor A. Hart,[2,3] Kevin S. Olsson [2,3,4] Matthew J. Turner,[2,3]
Jennifer M. Schloss,[5] and Ronald L. Walsworth[1,2,3]

[1]*Department of Physics, University of Maryland, College Park, Maryland 20742, USA*
[2]*Quantum Technology Center, University of Maryland, College Park, Maryland 20742, USA*
[3]*Department of Electrical Engineering and Computer Science,*
University of Maryland, College Park, Maryland 20742, USA
[4]*Intelligence Community Postdoctoral Research Fellowship Program,*
University of Maryland, College Park, Maryland 20742, USA
[5]*Lincoln Laboratory, Massachusetts Institute of Technology, Lexington, Massachusetts 02421, USA*

Nitrogen-vacancy (NV) spin ensembles in diamond provide an advanced magnetic sensing platform, with applications in both the physical and life sciences. The development of isotopically engineered ^{15}NV diamond offers advantages over naturally occurring ^{14}NV for magnetometry, due to its simpler hyperfine structure. However, for sensing modalities requiring a bias magnetic field not aligned with the sensing NV axis, the absence of a quadrupole moment in the ^{15}N nuclear spin leads to pronounced envelope modulation effects in time-dependent measurements of ^{15}NV spin evolution. While such behavior in spin echo experiments are well studied, analogous effects in Ramsey measurements and the implications for magnetometry remain underexplored. Here, we derive the modulated ^{15}NV Ramsey response to a misaligned bias field, using a simple vector description of the effective magnetic field on the nuclear spin. The predicted modulation properties are then compared to experimental results, revealing significant magnetic sensitivity loss if unaddressed. We demonstrate that double-quantum coherences of the NV $S = 1$ electronic spin states dramatically suppress these envelope modulations, while additionally proving resilient to other parasitic effects such as strain heterogeneity and temperature shifts.

I. INTRODUCTION

Ensembles of negatively charged nitrogen-vacancy (NV) centers in diamond are a leading quantum sensing platform, particularly for applications in magnetometry. The NV center has a magnetically sensitive electronic triplet ground state with spin $S = 1$ that can be optically initialized and read out, and coherently manipulated using microwave fields, while operating at ambient conditions.

Demonstrations of sensing or imaging of static and broadband (dc) magnetic fields have predominantly used continuous-wave optically detected magnetic resonance (CW-ODMR) techniques. However, the achievable volume-normalized magnetic sensitivity in CW-ODMR is constrained by competing effects of the optical and microwave fields applied during sensing [1]. Alternatively, pulsed measurement protocols such as Ramsey interference magnetometry can be employed to measure dc magnetic fields [2,3]. By separating spin control and readout from the sensing interval, pulsed measurements enable the use of increased optical and microwave intensities to improve sensitivity. As a result, some of the best volume-normalized dc sensitivities reported to date in NV ensembles (the sensitivity achieved per unit volume of interrogated diamond) were produced using Ramsey-based sensing protocols [4,5].

Beyond advancements in sensing protocols, the optimization of diamond material properties provides a crucial path towards improvements in volume-normalized sensitivity. In particular, ^{15}NV centers found in ^{15}N-enriched diamond provide practical advantages over the naturally abundant ^{14}NV due to the nuclear spin $I = 1/2$ of ^{15}N, as compared to $I = 1$ for ^{14}N. For sensing, this difference translates to increased signal contrast during optical readout while driving a single ^{15}NV hyperfine resonance, as the nuclear spin population is only distributed between two states. Both ^{15}NV hyperfine-split electronic resonances can also be driven simultaneously with the same Rabi nutation rate by tuning the frequency of the applied microwave field to the midpoint of the splitting, enabling more uniform spin control. In addition, the two-level nuclear spin system simplifies quantum logic protocols that exploit the coupled electron-nuclear system for enhanced sensing [6,7].

The ease with which Ramsey magnetometry can be implemented with ^{15}N-enriched diamond depends on the bias magnetic field commonly applied to break the ground state electronic spin degeneracy, associated with spin sublevels $m_s = \pm 1$. In practice, the bias field magnitude and orientation is often constrained by the desired sensing modality or system to be studied. For example, full vector reconstruction of magnetic fields in three dimensions typically requires a bias field oriented to produce a unique projection onto each class of NV centers across the four crystal axes [8–11]. This approach ensures that the resonances associated with each class

---

*jjoon@umd.edu
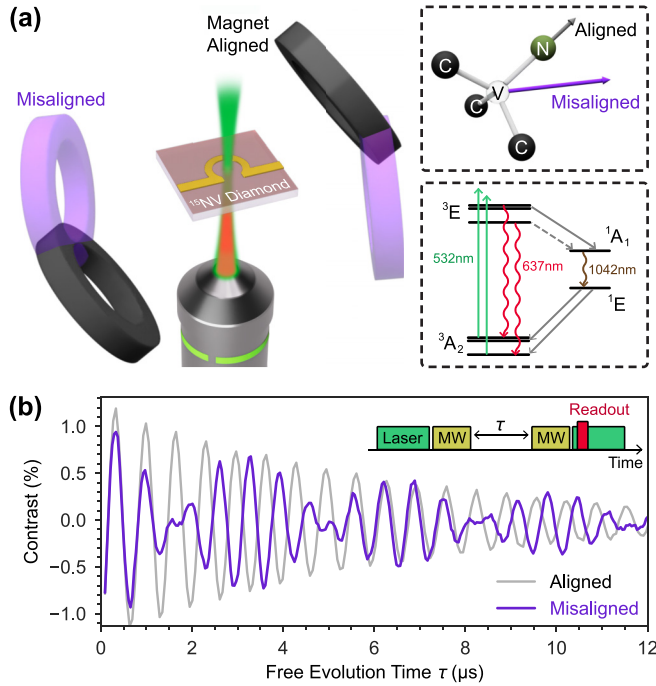†These authors contributed equally to this work.

FIG. 1. (a) Experimental setup schematic. Diamond containing an ensemble (≈ 0.3 ppm) of ^{15}NV centers is probed using 532 nm green laser excitation through a microscope objective, with red fluorescence collected back along the same path. A gold Ω-shaped waveguide is placed above the NV layer for microwave (MW) delivery. A pair of ring magnets apply a bias magnetic field at two distinct orientations, aligned and misaligned with the symmetry axis for one class of NV centers. Top right inset: diamond crystal axes and bias field orientations relative to a single NV quantization axis. Bottom right inset: NV electronic energy level diagram of ground and excited states. (b) Example Ramsey time series measured for bias fields aligned (gray) and misaligned (blue) to one class of NV centers. Effect of electron Ramsey envelope modulation (EREEM) is clearly observable for data with the misaligned field. Top inset: Ramsey pulse sequence diagram.

of NV centers are nondegenerate and individually addressable with microwave control. Alternatively, the bias field may be applied to spectrally overlap two or more NV classes to increase the number of spins participating in sensing, improving sensitivity [11–15].

In the presence of such misaligned fields (Fig. 1), we observe envelope modulations in ^{15}NV Ramsey measurements, which negatively impacts sensitivity if left unaddressed. The physical origin of this behavior can be attributed to the electron-nuclear hyperfine coupling of the ^{15}NV center in the presence of a transverse magnetic field. This effect resembles the well-known electron spin echo envelope modulation (ESEEM), which has received extensive study for over half a century in NMR systems and more recently in solid-state defects [16–18]. However, the analogous effect on a Ramsey measurement and the resulting impact on NV magnetic sensing has yet to be detailed.

In this paper, we characterize this effect, which we refer to as electron Ramsey envelope modulation or EREEM. First, we model the Ramsey envelope properties by considering an

NV electronic spin coupled to its native nitrogen nuclear spin. The resulting EREEM predictions are compared to experimental results, showing good agreement for ^{15}NV ensembles across a range of magnetic field magnitudes and misalignments. We then discuss the impact of EREEM on NV diamond magnetic sensitivity, considering typical operating conditions used for magnetometry. Finally we study EREEM in the context of double-quantum (DQ) protocols, which leverage superpositions of NV electronic spin states $|m_s = \pm 1\rangle$ for magnetometry. We demonstrate dramatic suppression of envelope modulations in DQ Ramsey measurements. These results provide further motivation for the use of DQ sensing schemes, in addition to their documented robustness to strain gradients and temperature drift [5,19–22].

II. ELECTRON RAMSEY ENVELOPE MODULATION (EREEM)

This section presents a derivation of EREEM properties, described by a simple vector model of the effective magnetic field on the nitrogen nuclear spin, which, importantly, is dependent on the NV electronic spin state. First, the ^{15}NV center is modeled by an electronic spin system ($S = 1$) coupled to the native ^{15}N nuclear spin ($I = 1/2$). Under the application of a bias magnetic field $\vec{B} = (B_x, B_y, B_z)$, the ground state Hamiltonian H can be written as [23]

$$\frac{H}{\hbar} = D\hat{S}_z^2 - \gamma_e \vec{B} \cdot \vec{S} - \gamma_n \vec{B} \cdot \vec{I} + \vec{S} \cdot \mathbf{A} \cdot \vec{I}. \quad (1)$$

The vectors $\vec{S} = (\hat{S}_x, \hat{S}_y, \hat{S}_z)$ and $\vec{I} = (\hat{I}_x, \hat{I}_y, \hat{I}_z)$ contain the electronic and nuclear spin operators, respectively, with corresponding gyromagnetic ratios $\gamma_e = 2\pi \times -2.8024$ MHz/G and $\gamma_n = 2\pi \times -431.6$ Hz/G. The room-temperature zero field splitting $D \approx 2\pi \times 2.87$ GHz [24] sets the electron quantization axis along $\hat{z}$. The NV hyperfine interaction is described by the diagonal tensor $\mathbf{A} = \begin{pmatrix} A_\perp & 0 & 0 \\ 0 & A_\perp & 0 \\ 0 & 0 & A_{||} \end{pmatrix}$, with transverse and longitudinal components $A_\perp = 2\pi \times 3.65$ MHz and $A_{||} = 2\pi \times 3.03$ MHz, respectively [25]. This ground state energy level structure is depicted in Fig. 2(a), for a magnetic field of magnitude B aligned along the $\hat{z}$ direction.

The C_{3v} symmetry of the NV center allows us to restrict the magnetic field to the x-z plane without any loss in generality [26]. For this study, we consider bias magnetic fields $B < 200$ G. Within this field regime, the zero field splitting term $D\hat{S}_z^2$ sets the dominant energy scale in the Hamiltonian, allowing us to treat contributions not commuting with S_z as nonsecular perturbations. Accurate to second order in perturbation theory, a leading-order correction to the secular Hamiltonian can be obtained [18,26,27]. After transforming into a frame resonant with the two electronic transitions $m_s = 0 \leftrightarrow +1$ and $0 \leftrightarrow -1$ [21], the following Hamiltonian under the rotating wave approximation is found:

$$\frac{\widetilde{H}}{\hbar} = A_{||}\hat{S}_z\hat{I}_z - \gamma_n B_z\hat{I}_z - (1 - 2\kappa)\gamma_n B_x\hat{I}_x - 3\kappa\gamma_n B_x\hat{S}_z^2\hat{I}_x. \quad (2)$$

Here, a dimensionless factor $\kappa \equiv \frac{\gamma_e A_\perp}{\gamma_n D} \approx 8.26$ describes an effective amplification of the bare nuclear spin response to a transverse magnetic field B_x, by a factor of $1 - 2\kappa \approx -15.5$.

(a)

(b)

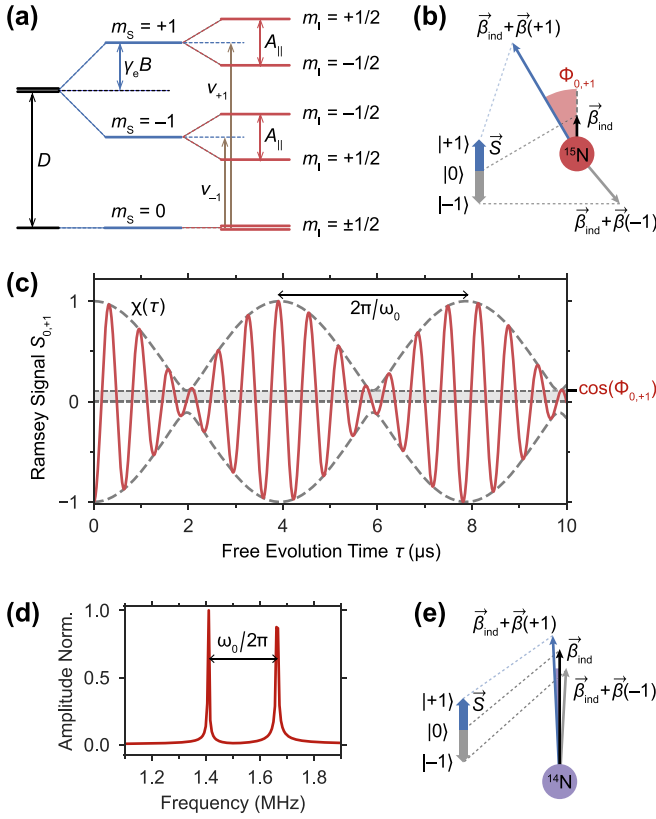
(c)

(d)

(e)

FIG. 2. (a) Energy level diagram for the ^{15}NV ground state, with splittings due to Zeeman and hyperfine interactions assuming an aligned bias field. The frequency of an applied microwave field ν_{+1} is centered between the two $m_s = 0 \leftrightarrow m_s = +1$ electronic resonances split by the NV hyperfine interaction. (b) Effective magnetic field vectors on the ^{15}N nuclear spin due to a misaligned bias magnetic field, for each electronic spin state $|m_s\rangle$. The nuclear spin experiences an effective magnetic field consisting of an electronic-spin-dependent contribution $\vec{\beta}(m_s)$, and a component $\vec{\beta}_{\mathrm{ind}}$ that is independent of the electronic spin state. (c) Example ^{15}NV Ramsey free induction signal due to a bias magnetic field of magnitude $B = 100\,\mathrm{G}$ at a misalignment of 22°, showing envelope modulation. The amplitude modulation $\chi(\tau)$ is indicated, showing oscillations between $\chi_{\min} = \cos(\Phi_{0,+1})$ and 1, with a characteristic period $2\pi/\omega_0$. (d) Amplitude spectrum of the Ramsey signal from (c), revealing two peaks split by the envelope beat frequency $\omega_0 = 2\pi \times 254\,\mathrm{kHz}$. (e) Effective magnetic field vectors on the ^{14}N nuclear spin. For all three electronic spin states, the corresponding effective fields on the nuclear spin are nearly parallel due to a dominant nuclear quadrupolar field.

The contributions to Eq. (2) can be separated into two categories. The first category consists of terms that depend on $\hat{S}_z$ or equivalently m_s. The sum of these terms can be described as an effective vector magnetic field $\vec{\beta}(m_s)$ on the nuclear spin. The terms that do not contain $\hat{S}_z$ can be represented by a spin-independent effective field $\vec{\beta}_{\mathrm{ind}}$, with a constant coupling to the nuclear spin regardless of the electronic spin state m_s. The resulting Hamiltonian can thus be summarized as

$$\frac{\widetilde{H}_n}{\hbar} = -\gamma_n(\vec{\beta}_{\mathrm{ind}} + \vec{\beta}(m_s)) \cdot \vec{I}. \qquad (3)$$

For a given electronic spin state $|m_s\rangle$, the nuclear spin precesses around an effective magnetic field $\vec{\beta}_{\mathrm{ind}} + \vec{\beta}(m_s)$ with a Larmor frequency

$$\omega_{m_s} = |\gamma_n(\vec{\beta}_{\mathrm{ind}} + \vec{\beta}(m_s))|. \qquad (4)$$

For $m_s = 0$ in particular, there are no terms in Eq. (2) that depend on the electronic spin state, such that $\vec{\beta}(0) = 0$ and $\omega_0 = |\gamma_n\beta_{\mathrm{ind}}|$. These field vectors are visualized in Fig. 2(b). For simplicity, the coordinate system is rotated so the spin-independent field $\vec{\beta}_{\mathrm{ind}} = \beta_{\mathrm{ind}}\hat{z}'$ now lies along the newly defined z' axis [27]. In this frame, the angle between $\vec{\beta}_{\mathrm{ind}}$ and an effective field $\vec{\beta}_{\mathrm{ind}} + \vec{\beta}(m_s)$ is given by

$$\phi_{m_s} = \tan^{-1}\left(\frac{\beta_{x'}(m_s)}{\beta_{\mathrm{ind}} + \beta_{z'}(m_s)}\right), \qquad (5)$$

where $\beta_{z'}(m_s)$ and $\beta_{x'}(m_s)$ denote components of $\vec{\beta}(m_s)$ parallel and perpendicular to $\hat{z}'$, respectively. For distinct electronic spin states $|i\rangle$ and $|j\rangle$, we define the angle between the two corresponding effective fields on the nuclear spin as $\Phi_{i,j}$, with the example $\Phi_{0,+1} = \phi_{+1}$ shown in Fig. 2(b).

Using this vector description, we derive the expected Ramsey envelope modulation as a function of the free evolution time τ. For an initial superposition of electronic spin states $|i\rangle$ and $|j\rangle$, the Ramsey signal $S_{i,j}(\tau)$, up to an overall phase, is given by

$$S_{i,j}(\tau) = \cos(\Phi_{i,j})\sin\left(\frac{\omega_i\tau}{2}\right)\sin\left(\frac{\omega_j\tau}{2}\right)$$
$$- \cos\left(\frac{\omega_i\tau}{2}\right)\cos\left(\frac{\omega_j\tau}{2}\right). \qquad (6)$$

As an example, Fig. 2(c) shows the expected Ramsey response $S_{0,+1}(\tau)$ for a bias field of magnitude $B = 100\,\mathrm{G}$ misaligned from the NV axis by an angle $\theta = 22°$. The Ramsey signal oscillation is modulated by an envelope with a slow characteristic beat frequency ω_0, i.e., an example of EREEM. The corresponding amplitude spectrum is shown in Fig. 2(d), revealing two peaks centered around $\omega_{+1}/2 \approx A_{||}/2 = 2\pi \times 1.515\,\mathrm{MHz}$, with a frequency splitting of magnitude ω_0. Experimentally, this behavior can be produced by tuning the frequency ν_{+1} of the applied microwave $\pi/2$ pulses to be centered between the two hyperfine-split resonances, resulting in detunings of equal magnitude $\approx A_{||}/2$ from each transition.

At any given time τ, the maximum Ramsey signal contrast is corrected by a multiplicative factor $\chi(\tau)$, due to this envelope modulation. This amplitude modulation factor $\chi(\tau)$ oscillates as a function of τ between values $\chi_{\min} = |\cos(\Phi_{0,+1})|$ and $\chi_{\max} = 1$, indicating points of minimum and maximum contrast, respectively. The depth of this modulation can be inferred from the angle $\Phi_{0,+1}$ between the participating effective fields on the nuclear spin.

To connect this vector model to the expected EREEM behavior in experimentally realistic conditions, we first consider a magnetic field aligned with the NV axis. Since $B_x = 0$, the Hamiltonian in Eq. (2) consists only of nuclear spin contributions along $\hat{I}_z$. In this case, the effective fields coupled to the nuclear spin, $\vec{\beta}_{\mathrm{ind}}$ and $\vec{\beta}_{\mathrm{ind}} + \vec{\beta}(+1)$, are parallel such that $\Phi_{0,+1} = 0$. No Ramsey envelope modulation should be observed, as the amplitude modulation factor remains constant:

$\chi_{\min} = |\cos(\Phi_{0,+1})| = \chi_{\max} = 1$. However, in the presence of a magnetic field not aligned with the NV axis ($B_x \neq 0$), the nuclear spin experiences an enhanced transverse magnetic field determined by the factor κ. The effective fields are no longer aligned, $\Phi_{0,+1} > 0$, which should lead to observable envelope modulation. At bias magnetic fields where $\vec{\beta}_{\text{ind}}$ and $\vec{\beta}_{\text{ind}} + \vec{\beta}(+1)$ are orthogonal, $\chi_{\min} = 0$ and the Ramsey signal contrast at modulation nodes is maximally suppressed.

This vector model can be readily extended to the ^{14}NV center, with some modifications. Besides straightforward changes to the physical constants $A_\perp$, $A_{||}$, and γ_n, an additional nuclear quadrupolar interaction term $Q\hat{I}_z^2$ contributes to the Hamiltonian in Eq. (1), with quadrupolar coupling constant $Q = 2\pi \times -4.945$ MHz [28,29]. This inclusion dramatically changes the Ramsey envelope properties, by contributing a large quantizing field of magnitude $|Q/\gamma_n| \approx 16\,000$ G to $\vec{\beta}_{\text{ind}}$ [18]. In the small magnetic field regime $B \ll |Q/\gamma_n|$, the effective fields $\vec{\beta}_{\text{ind}} + \vec{\beta}(m_s)$ coupled to the nuclear spin are dominated by the spin-independent contribution $\vec{\beta}_{\text{ind}}$, which is visualized in Fig. 2(e). The small angle between these field vectors results in $\chi_{\min} \approx 1$, and hence suppressed EREEM for ^{14}NV.

III. EXPERIMENTAL METHODS

The measurements for this study utilize a custom-built microscope setup and a $100\,\mu$m-thick, ^{15}N-enriched CVD diamond layer (NV $T_2^* = 5\,\mu$s, [N] $\approx$ 3 ppm, >99.995% ^{12}C), grown by Element Six Ltd. on a $2 \times 2 \times 0.5$ mm^3 high-purity diamond substrate, as shown in Fig. 1(a). Postgrowth treatment via electron irradiation and annealing increases the NV concentration to approximately 0.3 ppm.

Initialization of the NV ensemble electronic spin states is accomplished via pulsed 532 nm excitation, generated by a continuous-wave laser gated by an acoustic optical modulator (AOM). The light is focused onto the NV layer using a microscope objective, which is also used to route the outgoing NV fluorescence for spin-state readout. Microwave pulses are synthesized by signal generators and controlled by switches for single- or double-quantum control of the NV spin states. The microwave drive fields are delivered through an Ω-shaped planar waveguide, fabricated onto a sapphire substrate. The bias magnetic field is applied using two identical permanent ring magnets equally spaced from the diamond sample. The field magnitude is manually adjusted by varying the separation between the magnets. To control the field misalignment angle from the target NV axis, two automated rotation stages are used to adjust the yaw and pitch of the magnet pair with a nominal accuracy of $0.047°$. The bias magnets provide a homogeneous field magnitude of up to $\sim$150 G over an illumination spot size of $\sim$20 μm in diameter on the NV-rich layer. Additional details regarding the experimental setup are provided in the Supplemental Material [27].

To accurately determine the bias field magnitude B and misalignment angle θ, pulsed optically detected magnetic resonance (pulsed-ODMR) spectroscopy is employed to probe the NV ground state spin resonances. First, the field is aligned to a single NV axis by adjusting the magnets until the pulsed-ODMR spectra of the other three misaligned NV

classes overlap. Using weak microwave π pulses of duration $\sim$1 μs each [30], the resonance spectrum of the aligned NV axis is recorded for both electronic transitions $m_s = 0 \leftrightarrow +1$ and $m_s = 0 \leftrightarrow -1$. These transitions are separated by $\Delta_{\pm 1} = 2\gamma_e B$, which is used to estimate the bias field magnitude B. The magnets are then rotated away from the NV quantization axis, and Ramsey measurements are performed at a range of misalignment angles θ. At each position, the ODMR spectrum is again recorded to measure $\Delta_{\pm 1}$. This frequency difference is determined by the field projection along the NV axis, $\Delta_{\pm 1} = 2\gamma_e B \cos\theta$, which is then used to estimate θ. Additional details are provided in the Supplemental Material [27]. Field misalignment angles of up to $\theta \approx 40°$ can be accessed, limited by the geometrical constraints of the setup.

IV. MEASURED EREEM PROPERTIES

To study the properties of electron Ramsey envelope modulation (EREEM), we perform a series of single-quantum Ramsey experiments involving the electronic basis states $|m_s = 0\rangle$ and $|m_s = +1\rangle$ only (similar results are expected for experiments using $|m_s = 0\rangle$ and $|m_s = -1\rangle$). The envelope properties are extracted using fits to the measured Ramsey time series, repeated at various magnetic field magnitudes and misalignment angles, with results shown in Fig. 3. The Ramsey protocol consists of two microwave $\pi/2$ pulses, spaced by a variable free precession interval τ. We tune the frequency ν_{+1} of the applied microwave field to the center of the hyperfine splitting [27], as illustrated in Fig. 2(a). This results in equal detunings of approximate magnitude $A_{||}/2 = 2\pi \times 1.515$ MHz from each hyperfine transition, giving the characteristic Ramsey fringe frequency. When exposed to a misaligned bias field, an additional slow beating (EREEM) is observed, as shown by an example in Fig 3(a). (The Supplemental Material [27] presents data and analysis for the applied microwave field frequency not being equally detuned from the two hyperfine-split $m_s = 0 \leftrightarrow m_s = +1$ transitions.)

The measured Ramsey signals are fit to a modified form of Eq. (6), which incorporates an exponential decay $e^{-(\tau/T_2^*)^p}$ with a characteristic dephasing time T_2^* and stretch factor p. To further adapt the expression to experimental data, an overall amplitude scaling factor, a vertical offset, and phase offsets are all included in the fit function [27]. From the resulting fits, two frequencies ω_0 and ω_{+1} are obtained. The values for the envelope beat frequency ω_0 are plotted in Fig. 3(b), with 95% confidence intervals indicated by error bars [27,31]. For each magnetic field magnitude, theoretical predictions for ω_0 are also plotted as solid curves, obtained from the spin-independent contributions to Eqs. (2) and (3),

$$\omega_0 = |\gamma_n \beta_{\text{ind}}| = |\gamma_n|\sqrt{B_z^2 + (1 - 2\kappa)^2 B_x^2}$$

$$= |\gamma_n|B\sqrt{1 + 4(\kappa^2 - \kappa)\sin^2\theta}. \quad (7)$$

As expected from Eq. (7), the measured envelope beat frequency ω_0 increases with both the magnetic field magnitude B and misalignment angle θ.

Notably, small differences are observed between theoretical predictions of ω_0 [solid curves in Fig. 3(b)] and fits to experimental data, ranging from around 2%–6% across
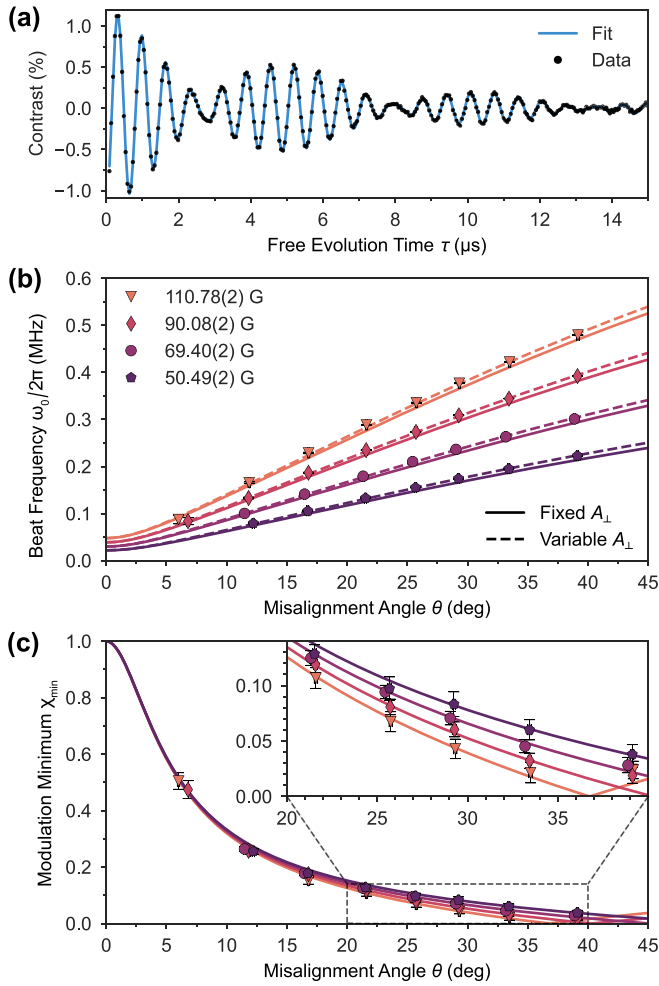
FIG. 3. Ramsey experimental data and envelope properties from model fits. (a) Example Ramsey time series at field magnitude $B = 90.08(2)$ G and misalignment angle $\theta = 16.79(9)°$. Data is shown in black and the fit in blue. The observed slow beating is an example of EREEM. (b) Estimates of envelope beat frequency ω_0 extracted from fits to experimental data, collected across a range of magnetic field magnitudes and orientations. Theoretical predictions for ω_0 are shown in solid lines for each magnetic field. After allowing the transverse hyperfine constant $A_\perp$ to vary as a fitting parameter, updated ω_0 predictions at each field are shown with dashed lines. (c) Estimates of the relative contrast at amplitude modulation nodes, χ_{min}, for the magnetic field configurations used in (b). Solid lines indicate theoretical predictions with $A_\perp$ fixed. Inset: Magnified view of χ_{min} values for misalignment angles $20° < \theta < 40°$.

the measurements presented in Fig. 3. To explore this inconsistency, we first perform full-Hamiltonian numerical simulations of Ramsey spin dynamics and compare the observed envelope beat frequency to Eq. (7), which was originally obtained using second-order perturbation theory. These simulations are conducted using the QUTIP package [32,33] in PYTHON. The NV system is described by the laboratory frame Hamiltonian from Eq. (1) and the pulse sequence is implemented using time-dependent ac magnetic field contributions. For the field configurations considered in Fig. 3, strong agreement is observed between Eq. (7) and the results of QUTIP simulations, with differences in $\omega_0 \lesssim 1\%$ (see the

Supplemental Material [27]). These results, however, do not fully account for the observed discrepancies in ω_0.

Interestingly, the agreement between analytical and experimental results is improved when the enhancement parameter $\kappa = \frac{\gamma_e A_\perp}{\gamma_n D}$ in Eq. (7) is allowed to deviate. Besides the transverse hyperfine constant $A_\perp$, other contributions to κ include the well-established gyromagnetic ratios γ_e and γ_n, and the zero field splitting D. We determine D to be 2870.71(4) MHz using pulsed-ODMR measurements, consistent ($< 0.03\%$ deviation) with the value assumed for analytical predictions and QUTIP numerical simulations. In contrast, an experimental determination of $A_\perp$ for ^{15}NV has (to our knowledge) only been reported once, by Felton et al. [25], using EPR studies at higher fields $B \sim 2000$ G. Given the simple relationship between the envelope beat frequency ω_0 and $A_\perp$ at low fields [via κ in Eq. (7)], EREEM presents a direct probe of $A_\perp$ in this regime. With this in mind, we conduct a phenomenological fit of Eq. (7) to measurements of ω_0 at each magnetic field, with $A_\perp$ as the sole degree of freedom. Using the adjusted $A_\perp$ values at each field, the corresponding values for ω_0 from Eq. (7) are shown as dashed lines in Fig. 3(b). We obtain values of $A_\perp/2\pi$ between 3.74 MHz and 3.80 MHz across the fields considered here, differing slightly from the previously reported value of 3.65(3) MHz by around 3%. Although such adjustments to $A_\perp$ reconcile the predictions from Eq. (7) with the results of experimental fits, we also observe a dependence on the bias magnetic field B [34,35], detailed further in the Supplemental Material [27]. This behavior warrants a more thorough study of EREEM across an extended range of magnetic fields, and is left as a subject for future work.

Figure 3(c) shows excellent agreement between theoretical predictions and experimentally observed values of the relative contrast at amplitude modulation nodes $\chi_{min} = |\cos(\Phi_{0,+1})|$. Even for modest misalignments of $\sim 10°$, the contrast at the nodes of the envelope modulation is reduced to around 30% of its maximum value. The resulting implications for magnetic field sensitivity are discussed in the following section.

V. MODULATION AMPLITUDE AND IMPACT ON MAGNETOMETRY

To study the impact of EREEM on NV magnetic field sensitivity, we first consider a conventional Ramsey magnetometry measurement in the absence of any envelope modulation, using a single-quantum coherence between states $|m_s = 0\rangle$ and either $|m_s = +1\rangle$ or $|m_s = -1\rangle$. After a Ramsey free evolution duration τ, this coherent superposition accumulates a relative phase $\phi \approx \gamma_e b_s \tau$ proportional to a magnetic field signal b_s along the NV axis [36]. The final $\pi/2$ pulse of each Ramsey sequence maps this phase onto changes in the NV electronic spin population, which can be detected using fluorescence contrast measurements at a fixed τ. This optimal working point τ is determined by optimizing the photon shot noise-limited sensitivity [1],

$$\eta = \frac{1}{\gamma_e} \frac{1}{Ce^{-(\tau/T_2^*)^p}\sqrt{N}} \frac{\sqrt{\tau + T_D}}{\tau}. \quad (8)$$

This calculation includes the maximum Ramsey fluorescence contrast C, obtained experimentally, which decays due to NV spin dephasing via a correction factor $e^{-(\tau/T_2^*)^p}$. The average
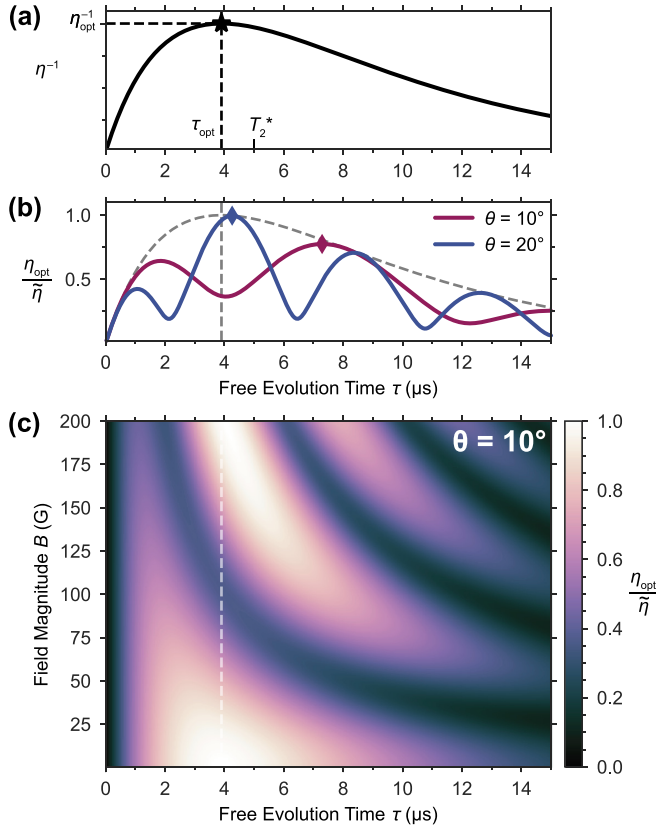
FIG. 4. Calculations of expected Ramsey magnetic field sensitivity with and without envelope modulation (EREEM), and at different bias magnetic field configurations. (a) Inverse sensitivity η^{-1} vs Ramsey free evolution time τ without EREEM, given by Eq. (9) for fixed dead time $T_D = 5\,\mu$s and dephasing time $T_2^* = 5\,\mu$s. The optimal inverse sensitivity η_{opt}^{-1} is indicated, corresponding to a free evolution time τ_{opt} indicated in all subfigures with a vertical dashed line. (b) Relative inverse sensitivity with EREEM $\eta_{\text{opt}}/\widetilde{\eta}$, normalized to the optimal sensitivity and free evolution time established in (a), for two distinct magnetic field misalignment angles $\theta = 10°, 20°$ at the fixed magnitude $B = 100$ G. Adjusted optimal evolution times $\widetilde{\tau}_{\text{opt}}$ are indicated by symbols $\Diamond$. (c) 2D color plot of the normalized inverse sensitivity at a fixed misalignment angle $\theta = 10°$, across bias field magnitudes $0 < B < 200$ G.

photon number is denoted by N and the dead time T_D represents the time spent outside the Ramsey sensing sequence for spin-state initialization and readout. A plot of η^{-1} as a function of τ is shown in Fig. 4(a), setting $p = 1$, $T_2^* = 5\,\mu$s, and $T_D = 5\,\mu$s according to our experimental conditions. This reveals an optimal sensitivity η_{opt} obtained at a corresponding free evolution time τ_{opt}, which approaches T_2^* in the limit of long overhead time $T_D \gg \tau$.

If EREEM is observed, then the contrast C takes on an additional correction factor due to the amplitude modulation $\chi(\tau)$, which results in an adjusted sensitivity $\widetilde{\eta}$. Normalizing to η_{opt}, the relative inverse sensitivity is therefore given by the following ratio, assuming N, T_2^*, p, and T_D remain unchanged between experiments:

$$\frac{\eta_{\text{opt}}}{\widetilde{\eta}} = \chi(\tau)\sqrt{\frac{\tau_{\text{opt}} + T_D}{\tau + T_D}} \exp\left(\frac{\tau_{\text{opt}} - \tau}{T_2^*}\right). \qquad (9)$$

As established earlier, $\chi(\tau)$ oscillates between values $\chi_{\min} = |\cos(\Phi_{0,\pm 1})|$ and $\chi_{\max} = 1$, at a characteristic beat frequency ω_0. These envelope properties are determined by the magnetic field magnitude B and misalignment angle θ, which in turn affect the relative inverse sensitivity $\eta_{\text{opt}}/\widetilde{\eta}$.

The optimal sensitivity $\widetilde{\eta}_{\text{opt}} = \eta_{\text{opt}}$ is only achieved when an envelope maximum $\chi_{\max}$ occurs at τ_{opt}, obtained when the beat frequency ω_0 is an integer multiple of $2\pi/\tau_{\text{opt}}$. If this condition is not satisfied, an updated optimal evolution time $\widetilde{\tau}_{\text{opt}}$ is necessary to minimize sensitivity degradation. These two scenarios are depicted in Fig. 4(b), which shows $\eta_{\text{opt}}/\widetilde{\eta}$ at two misalignment angles $10°$ and $20°$, for a field magnitude $B = 100$ G. The adjusted optimal evolution time $\widetilde{\tau}_{\text{opt}}$ for each case is marked, with a notable reduction in sensitivity seen in the $10°$ configuration. Similarly, changes in the field magnitude B can affect sensitivity. Fixing the misalignment angle at $10°$ as an example (see the Supplemental Material for other misalignment angles [27]), Fig. 4(c) shows $\eta_{\text{opt}}/\widetilde{\eta}$ across a range of magnetic field magnitudes B and free evolution times τ. Since the beat frequency ω_0 increases with the field magnitude B, the relative inverse sensitivity $\eta_{\text{opt}}/\widetilde{\eta}$ exhibits faster oscillations with respect to τ for higher fields. The sensitivity is optimized at fields where a Ramsey envelope maximum coincides with τ_{opt}, with the latter indicated by a dashed line in Fig. 4(c).

These calculations indicate that the sensitivity loss due to EREEM is highly dependent on changes in the bias field configuration. In practice, the tunability and control of such parameters depend on the specific sensing modality or application. For example, in experiments where an equal bias field projection on multiple NV axes is desired, the misalignment angle θ is highly constrained. Separately, there may be restrictions on the applied field magnitude B, for example, during studies of paramagnetic systems [8].

VI. DOUBLE-QUANTUM RAMSEY

As described in the previous section, envelope modulation (EREEM) in single-quantum (SQ) Ramsey experiments depends on the bias magnetic field configuration, and can result in significant magnetic field sensitivity loss. Alternatively, double-quantum (DQ) Ramsey protocols, which exploit the full NV spin-1 system, can circumvent the deleterious effects of EREEM. In fact, we observe a dramatic reduction of envelope modulation while using DQ coherence magnetometry. This behavior is illustrated in Figs. 5(a), 5(b) which depicts measured SQ and DQ Ramsey free induction decay signals and their corresponding amplitude spectra, at the same magnetic field configuration.

The DQ Ramsey protocol employs dual-tone microwave pulses with frequencies resonant with both the electronic transitions $m_s = 0 \leftrightarrow +1$ and $m_s = 0 \leftrightarrow -1$, often referred to as DQ pulses. Besides this change to the applied pulses, the DQ Ramsey sequence mirrors the SQ protocol and consists of a pair of DQ pulses separated by a free evolution interval τ. The first DQ pulse prepares an equal superposition of the electronic spin states $|+1\rangle$ and $|-1\rangle$. After the interval τ, a second DQ pulse maps the relative phase accumulated by these basis states onto the NV spin population, which is then read out optically.
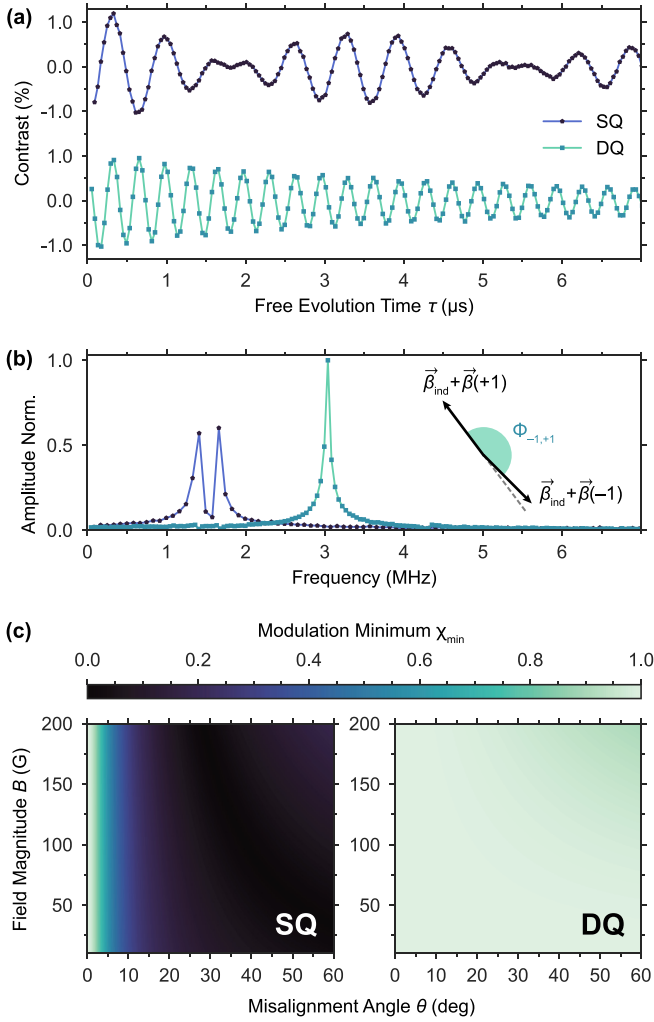
FIG. 5. Comparison between experimental single-quantum (SQ) and double-quantum (DQ) Ramsey measurements under a misaligned bias magnetic field. Representative SQ and DQ Ramsey data collected at a bias field magnitude $B \approx 50$ G and misalignment angle $\theta \approx 35°$, in both (a) time and (b) frequency domains. The inset in (b) shows the effective magnetic fields $\vec{\beta}_{ind} + \vec{\beta}(\pm 1)$ coupled to the nuclear spin, due to the electronic spin states $|m_s = \pm 1\rangle$ participating in the DQ protocol. The effective fields are nearly antiparallel ($\Phi_{-1,+1} \approx \pi$), resulting in no observable envelope modulation in the DQ Ramsey signal ($\chi_{min} = |\cos \Phi_{-1,+1}| \approx 1$). (c) Calculation of relative contrast at amplitude modulation nodes χ_{min} for both SQ and DQ Ramsey signals, over a range of bias magnetic field magnitudes and misalignment angles. For SQ Ramsey, calculated values of $\chi_{min} = |\cos \Phi_{0,+1}| = |\cos \phi_{+1}|$ are shown, obtained using Eq. (5). For DQ Ramsey, $\chi_{min} = |\cos \Phi_{-1,+1}| = |\cos (\phi_{+1} - \phi_{-1})|$.

The lack of EREEM in the observed DQ signal can be understood by referring back to the vector model established in Sec. II. The expected DQ Ramsey response can be described by Eq. (6) after substituting the electronic basis states denoted by i and j with -1 and $+1$, respectively. The effective nuclear magnetic fields associated with the electronic spin states $|m_s = \pm 1\rangle$ are then given by $\vec{\beta}_{ind} + \vec{\beta}(\pm 1)$ as depicted in Fig. 5(b). These field vectors are nearly antiparallel ($\Phi_{-1,+1} \approx \pi$), resulting in negligible enve-

lope modulation $\chi_{min} = |\cos (\Phi_{-1,+1})| \approx 1$ for a DQ Ramsey measurement.

The stark difference in envelope modulation behavior between SQ and DQ Ramsey is highlighted by calculations shown in Fig. 5(c). For a range of bias field magnitudes B and misalignment angles θ, the relative contrast at amplitude modulation nodes χ_{min} is plotted for both cases (see the Supplemental Material [27] for extended ranges of B and θ). Consistent with the results shown in Fig. 3(c), the SQ Ramsey contrast at envelope nodes decays rapidly as a function of θ, nearing zero even for small misalignment angles $\theta \sim 10°$. On the other hand, the DQ contrast is well preserved, with values of $\chi_{min} \approx 1$ across the fields considered in this work. Compared to SQ Ramsey, DQ Ramsey often provides more than an order of magnitude suppression of Ramsey amplitude modulation.

VII. CONCLUSION

In this work, we present a physical model of electron Ramsey envelope modulation (EREEM) and find reasonable agreement with experimental measurements using an ensemble of ^{15}NV centers in diamond. The observed envelope modulation exhibits a characteristic beat frequency and amplitude, dependent on the bias field magnitude and angle with respect to the NV quantization axis. We note a small systematic discrepancy between measurements of the envelope beat frequency and analytical predictions, which can be reconciled using an adjustment to the transverse hyperfine parameter $A_\perp$. These estimates deviate by around 3% from previous EPR measurements conducted at ~ 2000 G [25], an order of magnitude greater than the magnetic fields considered here. However, these estimates of $A_\perp$ exhibit a dependence on the applied field magnitude, warranting additional measurements across an extended range of magnetic fields in future studies.

For magnetic field sensing modalities requiring misaligned magnetic fields, the integration of ^{15}NV diamond and Ramsey coherence magnetometry is hindered by envelope modulation effects. We show that the resultant loss in sensitivity can be recovered by careful choice of the bias field. However, experimental constraints can limit the tunability of these field parameters. Alternatively, we find that double-quantum coherence magnetometry dramatically suppresses envelope modulation, while providing robustness to strain and temperature changes.

[1] J. F. Barry, J. M. Schloss, E. Bauch, M. J. Turner, C. A. Hart, L. M. Pham, and R. L. Walsworth, Sensitivity optimization for NV-diamond magnetometry, Rev. Mod. Phys. **92**, 015004 (2020).

[2] N. F. Ramsey, A molecular beam resonance method with separated oscillating fields, Phys. Rev. **78**, 695 (1950).

[3] L. Rondin, J.-P. Tetienne, T. Hingant, J.-F. Roch, P. Maletinsky, and V. Jacques, Magnetometry with nitrogen-vacancy defects in diamond, Rep. Prog. Phys. **77**, 056503 (2014).

[4] P. Balasubramanian, C. Osterkamp, Y. Chen, X. Chen, T. Teraji, E. Wu, B. Naydenov, and F. Jelezko, dc magnetometry with engineered nitrogen-vacancy spin ensembles in diamond, Nano Lett. **19**, 6681 (2019).

[5] C. A. Hart, J. M. Schloss, M. J. Turner, P. J. Scheidegger, E. Bauch, and R. L. Walsworth, N-*V*–Diamond Magnetic Microscopy Using a Double Quantum 4-Ramsey Protocol, Phys. Rev. Appl. **15**, 044020 (2021).

[6] I. Lovchinsky, A. O. Sushkov, E. Urbach, N. P. de Leon, S. Choi, K. D. Greve, R. Evans, R. Gertner, E. Bersin, C. Müller, L. McGuinness, F. Jelezko, R. L. Walsworth, H. Park, and M. D. Lukin, Nuclear magnetic resonance detection and spectroscopy of single proteins using quantum logic, Science **351**, 836 (2016).

[7] N. Arunkumar, K. S. Olsson, J. T. Oon, C. Hart, D. B. Bucher, D. Glenn, M. D. Lukin, H. Park, D. Ham, and R. L. Walsworth, Quantum logic enhanced sensing in solid-state spin ensembles, arXiv:2203.12501.

[8] D. R. Glenn, R. R. Fu, P. Kehayias, D. L. Sage, E. A. Lima, B. P. Weiss, and R. L. Walsworth, Micrometer-scale magnetic imaging of geological samples using a quantum diamond microscope, Geochem Geophys Geosyst **18**, 3254 (2017).

[9] J. M. Schloss, J. F. Barry, M. J. Turner, and R. L. Walsworth, Simultaneous Broadband Vector Magnetometry Using Solid-State Spins, Phys. Rev. Appl. **10**, 034044 (2018).

[10] M. J. Turner, N. Langellier, R. Bainbridge, D. Walters, S. Meesala, T. M. Babinec, P. Kehayias, A. Yacoby, E. Hu, M. Lončar, R. L. Walsworth, and E. V. Levine, Magnetic Field Fingerprinting of Integrated-Circuit Activity with a Quantum Diamond Microscope, Phys. Rev. Appl. **14**, 014097 (2020).

[11] E. V. Levine, M. J. Turner, P. Kehayias, C. A. Hart, N. Langellier, R. Trubko, D. R. Glenn, R. R. Fu, and R. L. Walsworth, Principles and techniques of the quantum diamond microscope, Nanophoton. **8**, 1945 (2019).

[12] K. Jensen, N. Leefer, A. Jarmola, Y. Dumeige, V. M. Acosta, P. Kehayias, B. Patton, and D. Budker, Cavity-Enhanced Room-Temperature Magnetometry Using Absorption by Nitrogen-Vacancy Centers in Diamond, Phys. Rev. Lett. **112**, 160802 (2014).

[13] J. F. Barry, M. J. Turner, J. M. Schloss, D. R. Glenn, Y. Song, M. D. Lukin, H. Park, and R. L. Walsworth, Optical magnetic detection of single-neuron action potentials using quantum defects in diamond, Proc. Natl. Acad. Sci. USA **113**, 14133 (2016).

[14] T. Lenz, G. Chatzidrosos, Z. Wang, L. Bougas, Y. Dumeige, A. Wickenbrock, N. Kerber, J. Zázvorka, F. Kammerbauer, M. Kläui, Z. Kazi, K.-M. C. Fu, K. M. Itoh, H. Watanabe, and D. Budker, Imaging Topological Spin Structures Using Light-Polarization and Magnetic Microscopy, Phys. Rev. Appl. **15**, 024040 (2021).

[15] S. T. Alsid, J. M. Schloss, M. H. Steinecker, J. F. Barry, A. C. Maccabe, G. Wang, P. Cappellaro, and D. A. Braje, A solid-state microwave magnetometer with picotesla-level sensitivity, arXiv:2206.15440.

[16] L. G. Rowan, E. L. Hahn, and W. B. Mims, Electron-spin-echo envelope modulation, Phys. Rev. **137**, A61 (1965).

[17] T. Gaebel, M. Domhan, I. Popa, C. Wittmann, P. Neumann, F. Jelezko, J. R. Rabeau, N. Stavrias, A. D. Greentree, S. Prawer, J. Meijer, J. Twamley, P. R. Hemmer, and J. Wrachtrup, Room-temperature coherent coupling of single spins in diamond, Nature Phys. **2**, 408 (2006).

[18] L. Childress, M. V. G. Dutt, J. M. Taylor, A. S. Zibrov, F. Jelezko, J. Wrachtrup, P. R. Hemmer, and M. D. Lukin, Coherent dynamics of coupled electron and nuclear spin qubits in diamond, Science **314**, 281 (2006).

[19] F. Reinhard, F. Shi, N. Zhao, F. Rempp, B. Naydenov, J. Meijer, L. T. Hall, L. Hollenberg, J. Du, R.-B. Liu, and J. Wrachtrup, Tuning a Spin Bath through the Quantum-Classical Transition, Phys. Rev. Lett. **108**, 200402 (2012).

[20] K. Fang, V. M. Acosta, C. Santori, Z. Huang, K. M. Itoh, H. Watanabe, S. Shikata, and R. G. Beausoleil, High-Sensitivity Magnetometry Based on Quantum Beats in Diamond Nitrogen-Vacancy Centers, Phys. Rev. Lett. **110**, 130802 (2013).

[21] H. J. Mamin, M. H. Sherwood, M. Kim, C. T. Rettner, K. Ohno, D. D. Awschalom, and D. Rugar, Multipulse Double-Quantum Magnetometry with Near-Surface Nitrogen-Vacancy Centers, Phys. Rev. Lett. **113**, 030803 (2014).

[22] E. Bauch, C. A. Hart, J. M. Schloss, M. J. Turner, J. F. Barry, P. Kehayias, S. Singh, and R. L. Walsworth, Ultralong Dephasing Times in Solid-State Spin Ensembles via Quantum Control, Phys. Rev. X **8**, 031025 (2018).

[23] M. W. Doherty, N. B. Manson, P. Delaney, F. Jelezko, J. Wrachtrup, and L. C. Hollenberg, The nitrogen-vacancy colour centre in diamond, Phys. Rep. **528**, 1 (2013).

[24] V. M. Acosta, E. Bauch, M. P. Ledbetter, A. Waxman, L.-S. Bouchard, and D. Budker, Temperature Dependence of the Nitrogen-Vacancy Magnetic Resonance in Diamond, Phys. Rev. Lett. **104**, 070801 (2010).

[25] S. Felton, A. M. Edmonds, M. E. Newton, P. M. Martineau, D. Fisher, D. J. Twitchen, and J. M. Baker, Hyperfine interaction in the ground state of the negatively charged nitrogen vacancy center in diamond, Phys. Rev. B **79**, 075203 (2009).

[26] B. Myers, Ph.D. thesis, University of California, Santa Barbara, 2016.

[27] See Supplemental Material at http://link.aps.org/supplemental/10.1103/PhysRevB.106.054110 for additional details.

[28] B. Smeltzer, J. McIntyre, and L. Childress, Robust control of individual nuclear spins in diamond, Phys. Rev. A **80**, 050302(R) (2009).

[29] M. Steiner, P. Neumann, J. Beck, F. Jelezko, and J. Wrachtrup, Universal enhancement of the optical readout fidelity of single electron spins at nitrogen-vacancy centers in diamond, Phys. Rev. B **81**, 035205 (2010).

[30] A. Dréau, M. Lesik, L. Rondin, P. Spinicelli, O. Arcizet, J.-F. Roch, and V. Jacques, Avoiding power broadening in optically detected magnetic resonance of single nv defects for enhanced dc magnetic field sensitivity, Phys. Rev. B **84**, 195204 (2011).

[31] T. J. DiCiccio and B. Efron, Bootstrap confidence intervals, Stat. Sci. **11**, 189 (1996).

[32] J. Johansson, P. Nation, and F. Nori, QuTiP: An open-source python framework for the dynamics of open quantum systems, Comput. Phys. Commun. **183**, 1760 (2012).

[33] J. Johansson, P. Nation, and F. Nori, QuTiP 2: A python framework for the dynamics of open quantum systems, Comput. Phys. Commun. **184**, 1234 (2013).

[34] M. Chen, M. Hirose, and P. Cappellaro, Measurement of transverse hyperfine interaction by forbidden transitions, Phys. Rev. B **92**, 020101(R) (2015).

[35] S. Sangtawesin, C. A. McLellan, B. A. Myers, A. C. B. Jayich, D. D. Awschalom, and J. R. Petta, Hyperfine-enhanced gyromagnetic ratio of a nuclear spin in diamond, New J. Phys. **18**, 083016 (2016).

[36] J. M. Taylor, P. Cappellaro, L. Childress, L. Jiang, D. Budker, P. R. Hemmer, A. Yacoby, R. Walsworth, and M. D. Lukin, High-sensitivity diamond magnetometer with nanoscale resolution, Nature Phys. **4**, 810 (2008).